Supplementary information

CeO_2 Promotes Oxygen Vacancy Generation in $Co(OH)_2$ for Enhanced Water Oxidation

Zidong He,[a] Zhaori Mu,[a] Peiqiong Li,[a] Yana Liu,[a] Yunxiang Zhang,[a] Wei Shen,[a] Pinxian Xi *[a] and

Chun-Hua Yan [ab]

[a]State Key Laboratory of Natural Product Chemistry, Key Laboratory of Nonferrous Metal Chemistry and Resources Utilization of Gansu Province, Frontiers Science Center for Rare Isotopes, College of Chemistry and Chemical Engineering, Lanzhou University Lanzhou 730000, China.

[b]Beijing National Laboratory for Molecular Sciences, State Key Laboratory of Rare Earth Materials Chemistry and Applications, PKU-HKU Joint Laboratory in Rare Earth Materials and Bioinorganic Chemistry, College of Chemistry and Molecular Engineering, Peking University, Beijing 100871, China.

*E-mail: xipx@lzu.edu.cn

Contents

1. Experimental Section

1.1 Materials

Cobalt nitrate hexahydrate ($Co(NO_3)_2 \cdot 6H_2O$, 99.99%, Innochem, China), cerium nitrate hexahydrate ($Ce(NO_3)_3 \cdot 6H_2O$, 99.99%, Adamas-beta, China), sodium chloride (NaCl, 99.5%, Kelong, China), potassium hydroxide (KOH, 99.99%, Aladdin, China), and tetramethylammonium hydroxide solution (TMAOH, $C_4H_{13}NO$, AR, 25% in water, Innochem, China) were used as received without further purification. Ultrapure water (resistivity: 18.25 MΩ·cm) for all solutions was obtained from a laboratory ultrapure water system (IA-30XV, Yihan, China).

Hydrophilic carbon paper (CP, TGPH060H) was purchased from SCI Materials Hub. Prior to use, it was cut into 0.5 × 2 cm^2 strips and sequentially sonicated for 20 min each in 3 M hydrochloric acid, ultrapure water, acetone, and ultrapure water. Subsequently, it was then immersed in sulfuric acid, thoroughly rinsed with ultrapure water, and dried overnight at 45 °C.

1.2 Materials Synthesis

Synthesis of $Co(OH)_2$-CeO_2 heterostructure: $Co(OH)_2$ was obtained via an electrodeposition method. Treated CP was masked with polyimide tape define an exposed deposition area of 0.5 × 1 cm^2. The masked CP served as the working electrode and immersed in 0.1 M $Co(NO_3)_2$ for a period of time. After sufficient wetting of the CP, electrodeposition was performed at -5 $mA \cdot cm^{-2}$ for 60 s. The resulting $Co(OH)_2$/CP was then dried briefly at 45 °C. Subsequently, a mixed solution of 2 mM $Ce(NO_3)_3$ and 10 mM NaCl was used as the electrolyte for the electrodeposition of CeO_2.[1] The $Co(OH)_2$-CeO_2 heterostructure was obtained by electrodepositing CeO_2 onto $Co(OH)_2$/CP at 0.25 $mA \cdot cm^{-2}$ for 600 s.

Synthesis of CoOOH-CeO_2 heterostructure: The synthesis of CoOOH-CeO_2 followed the same procedure as $Co(OH)_2$-CeO_2, except for an additional electrochemical conversion step. Specifically, after electrochemical activation, $Co(OH)_2$/CP was electrochemically converted to CoOOH/CP in 1 M KOH by cycling the potential between -0.1 and 0.8 V vs. Hg/HgO at a scan rate of 10 $mV \cdot s^{-1}$ for 3 cycles.

In this work, "CoOOH" refers to the electrochemically converted CoOOH/CP obtained by the above procedure, without subsequent CeO_2 electrodeposition.

We note that Sung et al.[22] prepared catalysts by depositing $Co(OH)_2$ onto CeO_2 and CeO_2 functioned as the primary phase (the "substrate" in our terminology) and $Co(OH)_2$ as the secondary phase. In contrast, we adopted the inverse approach by depositing CeO_2 onto $Co(OH)_2$ and CoOOH. In this situation, CeO_2 was served as a fixed secondary phase. This reversal allowed us to systematically investigate how substrate nature influences the magnitude of property enhancement provided by the same secondary phase.

1.3 Materials Characterizations

X-ray diffraction (XRD) patterns were acquired on a Rigaku MiniFlex 600 diffractometer equipped with Cu Kα radiation (λ = 0.1542 nm) at 40 kV, over a 2θ range of 10-70°. Morphology and quantitative energy dispersive X-ray spectroscopy (EDS) analyses were performed using a Thermo Fisher Apreo S field-emission scanning electron microscope (FE-SEM) operated at an acceleration voltage of 30 kV. Transmission electron microscopy (TEM) and high-resolution TEM (HR-TEM) images were captured by a Thermo Fisher Scientific Talos F200X G2 field-emission transmission electron microscope. Electron paramagnetic resonance (EPR) spectra were collected

at room temperature on a JES-FA300 spectrometer. X-ray photoelectron spectroscopy (XPS) measurements were conducted on a Kratos Axis Supra instrument, with binding energies calibrated to the C 1s peak at 284.3 eV. Raman spectra were collected using a LabRAM HR Evolution microscopy system (Horiba Jobin Yvon) equipped with a 473 nm laser and a 50× objective lens (Olympus LMPlanFL N, Japan).

1.4 Electrochemical Measurements

The electrcatalytic performance of the materials was evaluated at 25°C in 1 M KOH using an Ivium-n-Stat electrochemical workstation (Ivium Technologies, The Netherlands) in a three-electrode configuration with Kelvin sensing, where the composite electrode, Pt sheet, and a Hg/HgO electrode served as working , counter electrode, and reference electrodes, respectively, In situ electrochemical impedance spectroscopy (EIS) measurements were performed on a Gamry 5000E (Gamry Instruments, USA) by varying the applied potential to obtain the potential-dependent impedance response over a frequency range of 0.05 Hz - 100 kHz. Prior to electrochemical testing, the open-circuit potential (OCP) was monitored for at least 2 min to ensure system stability.

The potential difference between the Hg/HgO reference electrode and the reversible hydrogen electrode (RHE) was determined experimentally under the same conditions as used for all electrochemical measurements.[2] Pt wires served as both the working and counter electrodes in 1.0 M KOH electrolyte saturated with high-purity H_2 gas (99.999%) for at least 30 min before and during the measurement. Cyclic voltammetry (CV) scans were recorded at 1 $mV \cdot s^{-1}$ over the hydrogen evolution/oxidation potential region. The average of the two zero-current potentials from the forward and reverse scans was taken as the equilibrium potential. Accordingly, the calibration of the RHE using the equilibrium potential was expressed as:

$$E_{RHE} = E_{Hg/HgO} + 0.9238\ V$$

Prior to the performance testing, the electrodes were electrochemically activated by cycling 20 times between 0 and 0.5 V vs. Hg/HgO at a scan rate of 50 $mV \cdot s^{-1}$. All linear sweep voltammetry (LSV) measurements (at 10 $mV \cdot s^{-1}$) were corrected for 100% iR-drop. The uncompensated resistance (R_u) was obtained from EIS measurements at the same non-Faradaic potential. Chronopotentiometry and CV measurements (at 10 $mV \cdot s^{-1}$) were performed using the same electrode configuration. Double-layer capacitance (Cdl) was determined to estimate the electrochemically active surface area (ECSA) of the catalyst in 1 M KOH.[3] Specifically, voltammetric measurements were performed within the non-Faradaic potential region at different scan rates. At each vertex potential, the working electrode was held for 30 s prior to initiating the subsequent sweep to ensure surface stabilization. Electrochemical quartz crystal microbalance (eQCM) measurements were executed on the eQCM 15M (Gamry instruments, USA).

1.5 In Situ Spectroscopic Measurements

In situ Raman measurements: In situ Raman spectroscopy was performed using a custom-designed three-electrode cell. The Au substrates were cleaned and used to enhance the Raman signal intensity. Catalysts were directly electrodeposited onto the Au substrates to serve as working electrodes, with a Pt wire and an Ag/AgCl electrode as the counter and reference electrodes, respectively. A CHI-760E potentiostat (Shanghai Chenhua Instruments, China) was used to control the applied potential. Spectral calibration was performed using a silicon wafers reference (520.6

cm^{-1}). Each spectrum was collected over 30 s following a 2 min stabilization period at the applied potential.

In situ UV-Vis measurements: In situ ultraviolet-visible (UV-Vis) spectroscopy was carried out using a UV-2600 spectrophotometer (Shimadzu, Japan) integrated with a custom-built electrochemical cell as we reported earlier.[4] Catalysts were electrodeposited onto 2 × 2 cm^2 fluorine-doped tin oxide (FTO) substrates, with incident light transmitted through the FTO layer and the resulting signal converted into an optical absorption spectrum. A Pt wire and an Ag/AgCl electrode served as the counter and reference electrodes, respectively. The potential of the FTO-supported catalyst was controlled by a BioLogic SP150e potentiostat (BioLogic, France). Background spectra were ccollected at OCP, followed by full absorption spectrum acquisition during chronopotentiometric testing. To capture potential-induced optical changes, absorbance at a fixed wavelength of 600 nm was first recorded at OCP as a baseline. A series of short potential steps was then applied, and the resulting absorbance values were expressed as changes (ΔA) relative to the OCP baseline.[5] This approach allowed quantitative correlation of ΔA at 600 nm with shifts in the cobalt valence states under different applied potentials.

In situ ATR-SEIRAS measurements: In situ attenuated total reflection surface-enhanced infrared absorption spectroscopy (ATR-SEIRAS) wase performed in an optimized electrochemical cell. Catalysts were electrodeposited onto an Au-coated Si prism and served as the working electrode. A Pt sheet and an Ag/AgCl electrode were used as the counter and reference electrodes, respectively. Spectra were collected using a Bruker Invenio S Fourier transform infrared spectrometer equipped with a liquid nitrogen-cooled mercury-cadmium-telluride (MCT) detector and ATR optical accessories. A BioLogic SP150e electrochemical workstation (BioLogic, France) was employed to control the applied potentials from OCP to OER potentials. All measurements were conducted in 1 M KOH. Each absorption spectrum was obtained by averaging 64 scans at a resolution of 4 cm^{-1}.

1.6 Notes on Peak Assignments

Raman peak assignments: Unlike Co_3O_4, whose Raman bands can be clearly assigned, the spectra of $Co(OH)_2$ and CoOOH exhibit severe peak overlap and broad peak, complicating peak assignments. Yang et al. further proposed that peak assignments for $Co(OH)_2$ strongly depend on its state and varies with deposition amount.[6] Their work also employed multi-component fitting of Raman spectra, analogous to XPS peak deconvolution. We believe this approach better capture sample heterogeneity. Therefore, based on distinct peak shapes compared to cobalt oxides and combined with XRD analysis, we ruled out the formation of cobalt oxides and concluded that hydroxide predominates in the material. (Because we cannot observe the four distinct vibrational modes characteristic of the Co_3O_4 structure at 686 cm^{-1} (A_{1g}), 616 cm^{-1} (F_{2g}), 519 cm^{-1} (F_{2g}), and 481 cm^{-1} (E_g) in the Raman spectra.)

~600 cm^{-1} board band and surface evolution: Due to ongoing debates regarding peak assignment in this region, we have adopted a cautious way that does not affect the conclusions of our study. In some literature on CoOOH, Raman peaks at ~500 cm^{-1} and ~600 cm^{-1} have been assigned to the E_g and A_{1g} vibrations of Co-O, respectively.[7,8] However, Zhang et al.[9] in their study of β-$Co(OH)_2$ and Jing et al.[10] in their dedicated Raman work abandoned this simplified assignment. They favor the interpretation that the ~600 cm^{-1} peak reflects a valence state change which is consistent with thermodynamic principles. Even studies that attempt peak attribution acknowledge that shifts in the ~600 cm^{-1} band primarily reflect changes in cobalt valence state or

the formation of active sites, indicating that such attributions do not necessarily yield deeper insight than the valence-based interpretation.[7,8] Based on our experimental observations and a review of current literature, we find that the framework proposed by Yang et al.[6] remains valid: the broad band spanning 530-700 cm^{-1} should be considered as comprising multiple underlying peaks. Its shape reflects the evolving composition of different vibrational modes and should not be assigned to a single vibration. The peak shifts mentioned in the main text are a simplification, where the apparent shift of the broad envelope indicates the increasing dominance of a particular component within this composite band.

2. Supplementary Figures

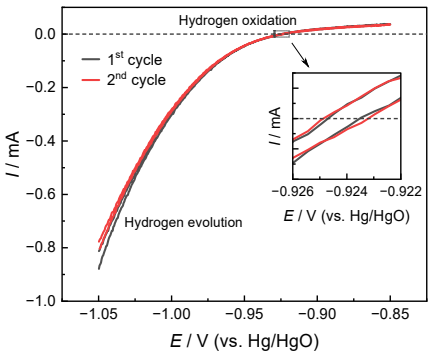

Figure S1. RHE calibration in 1 M KOH. CVs were run at a scan rate of 1 mV·s^{-1}.[2]

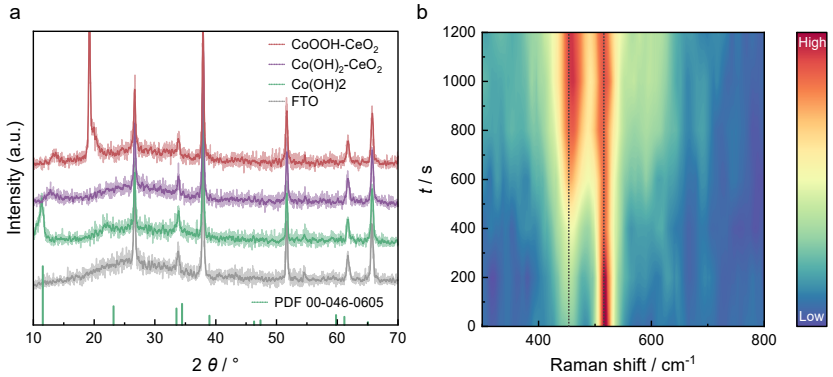

Figure S2. XRD patterns of bare FTO, $Co(OH)_2$/FTO, $Co(OH)_2$-CeO_2/FTO and CoOOH-CeO_2/FTO. (b) In situ Raman of CeO_2 deposition on $Co(OH)_2$ with varied time. (As the deposition time increases, a new peak can be observed.)

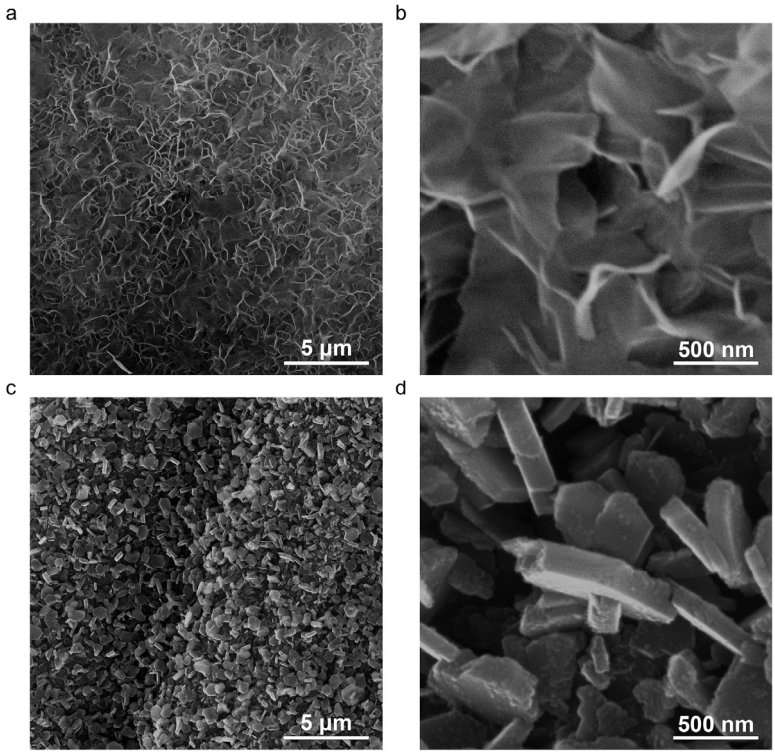

Figure S3. SEM images of (a, b) $Co(OH)_2$/CP and (c, d) CoOOH/CP.

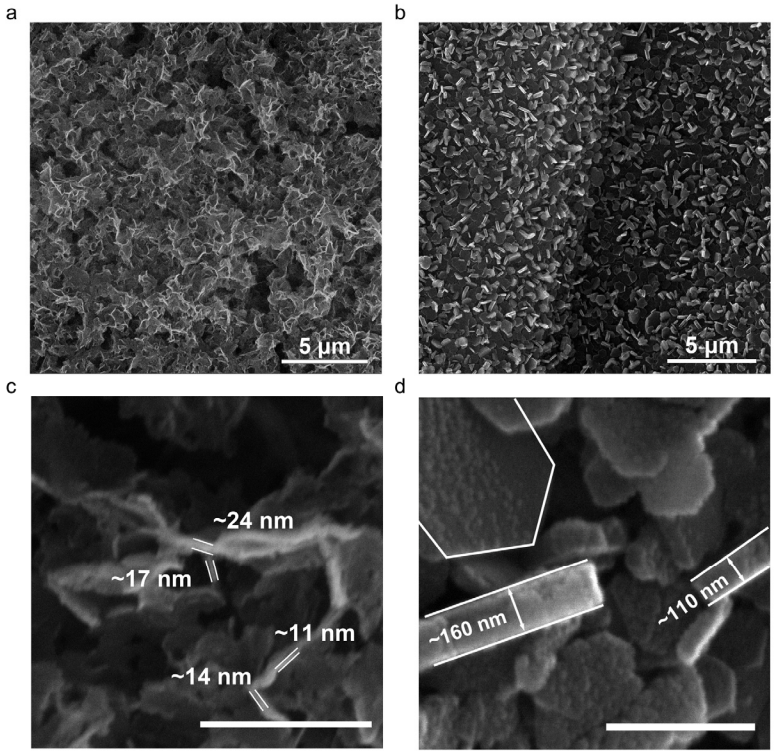

Figure S4. SEM images of (a) $Co(OH)_2$-CeO_2/CP and (b) CoOOH-CeO_2/CP before OER redox cycling. Annotated SEM images of (c) $Co(OH)_2$-CeO_2/CP and (d) CoOOH-CeO_2/CP. Thickness values are labeled in each image. Scale bars = 500 nm.

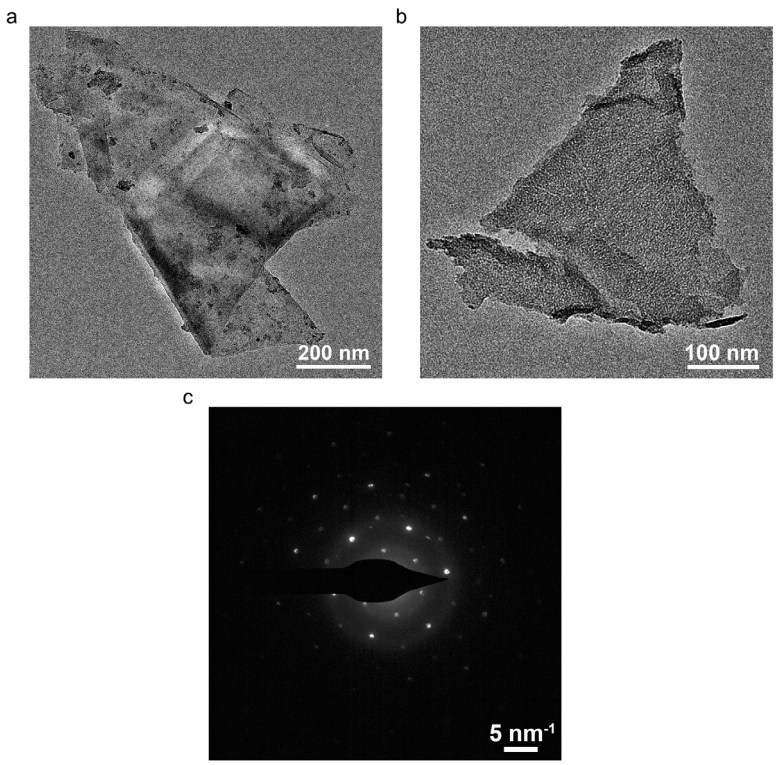

Figure S5. (a, b) TEM and (c) SAED images of $Co(OH)_2$-CeO_2 before OER redox cycling.

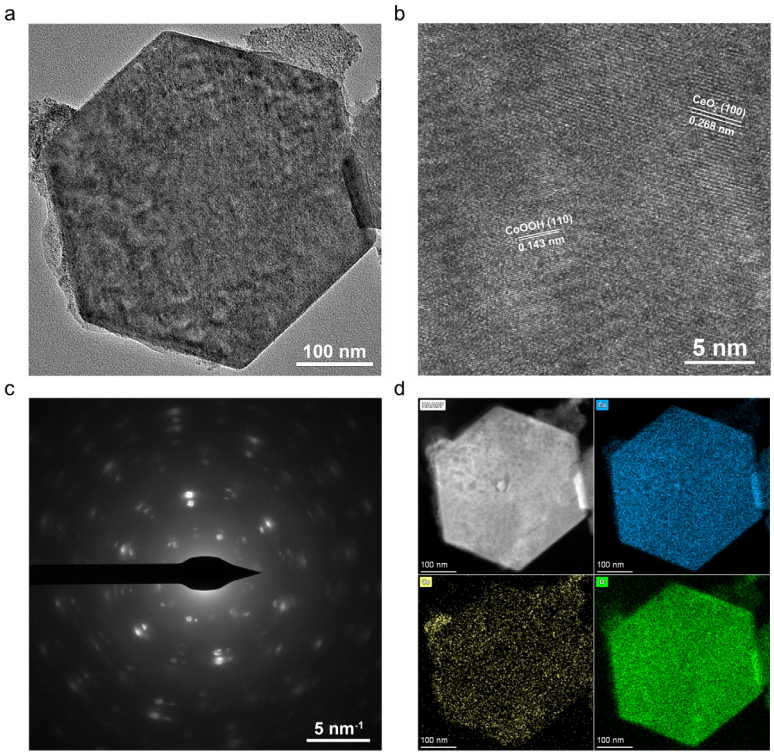

Figure S6. (a) TEM, (b) HRTEM, (c) SAED and (d) STEM-EDS images of CoOOH-CeO_2 before OER redox cycling.

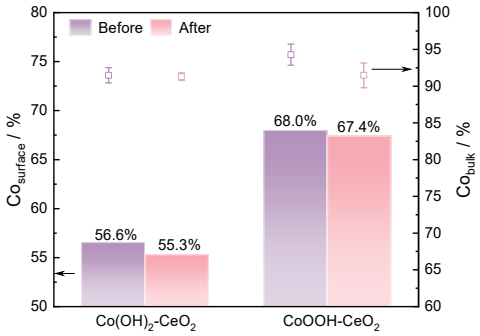

Figure S7. The proportion of Co in the total metal elements. Statistical analysis results based on XPS and SEM-EDS. The error bar was calculated based on five different regions.

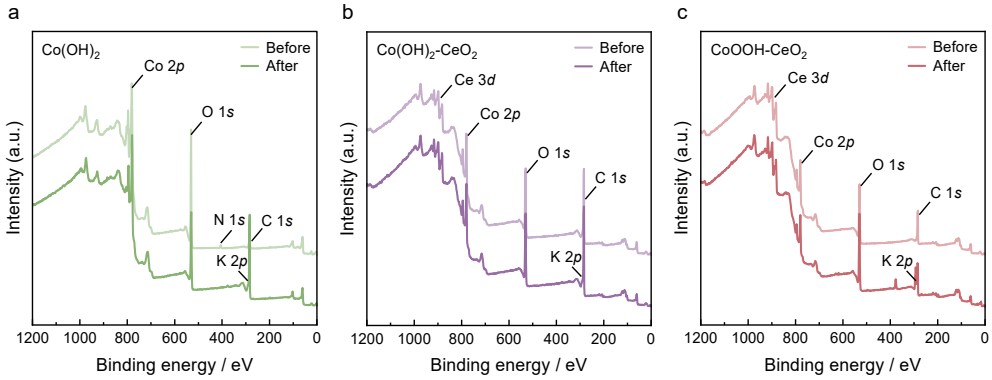

Figure S8. XPS wide-scan spectra of (a) $Co(OH)_2$, (b) $Co(OH)_2$-CeO_2 and (c) CoOOH-CeO_2 before and after OER redox cycles.

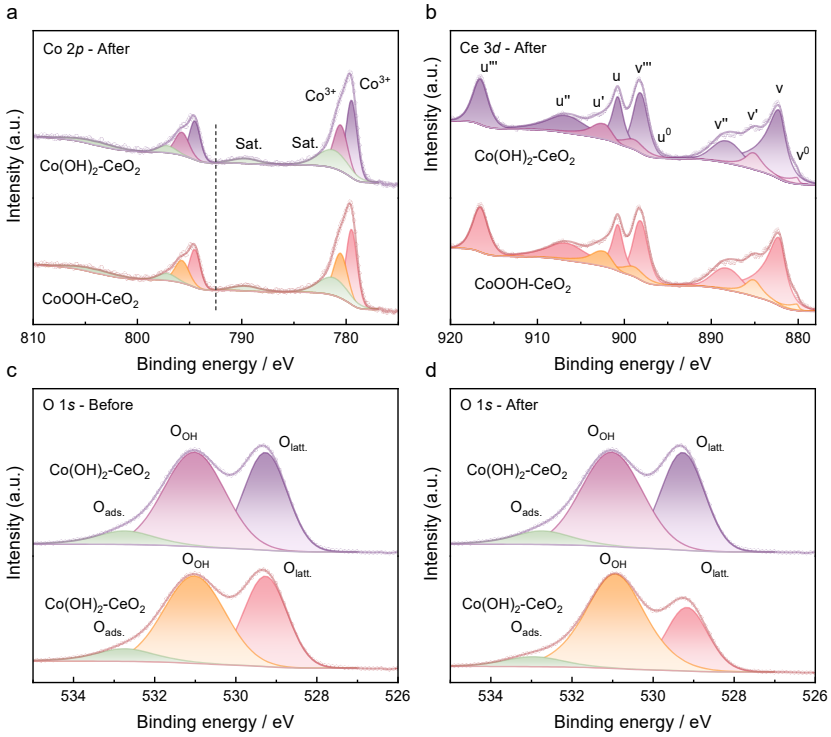

Figure S9. High resolution XPS spectra of (a) Co 2*p* and (b) Ce 3*d* with corresponding peak fitting of $Co(OH)_2$-CeO_2 and CoOOH-CeO_2 after OER redox cycling. O 1*s* with corresponding peak fitting of $Co(OH)_2$-CeO_2 and CoOOH-CeO_2 (c) before OER redox cycling and (d) after OER redox cycling.

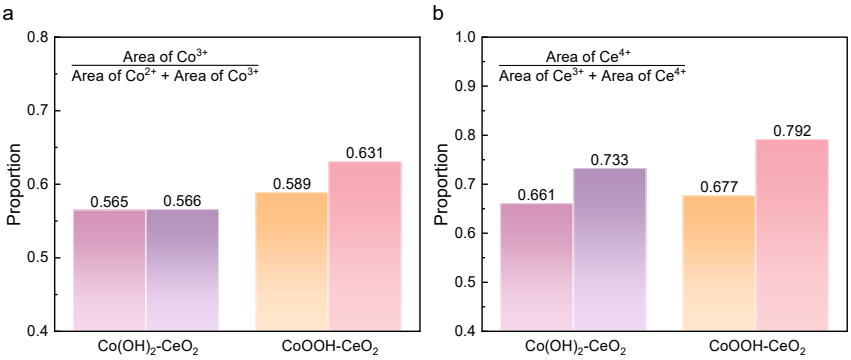

Figure S10. Ratio of (a) Co^{3+} and (b) Ce^{4+} from XPS analyses.

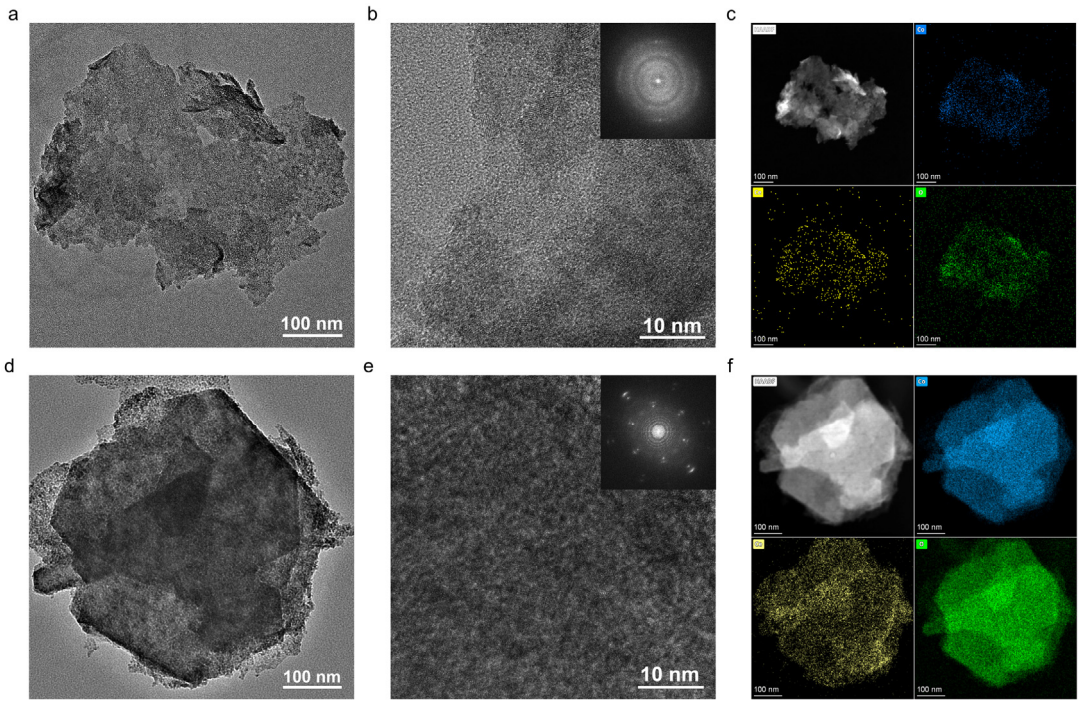

Figure S11. TEM, HRTEM (inset: the corresponding FFT image) and STEM-EDS images of (a, b, c) $Co(OH)_2$-CeO_2 and (d, e, f) CoOOH-CeO_2 after OER redox cycling.

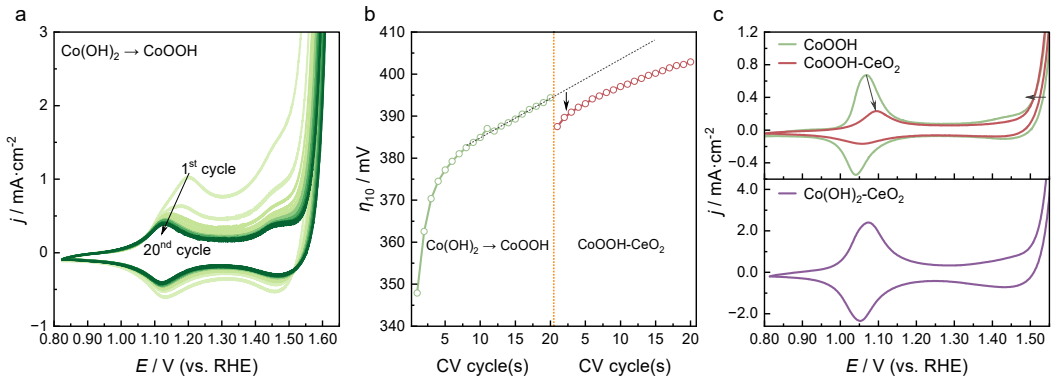

Figure S12. (a) CV curves of $Co(OH)_2$ at a scan rate of 10 $mV \cdot s^{-1}$ after *iR*-correction in 1 M KOH. (b) Overpotentials at 10 $mA \cdot cm^{-2}$ (η_{10}) extracted from the respective CV curves. (c) CV curves showing the Co^{2+}/Co^{3+} and Co^{3+}/Co^{4+} redox features at a scan rate of 10 $mV \cdot s^{-1}$ after *iR*-correction.

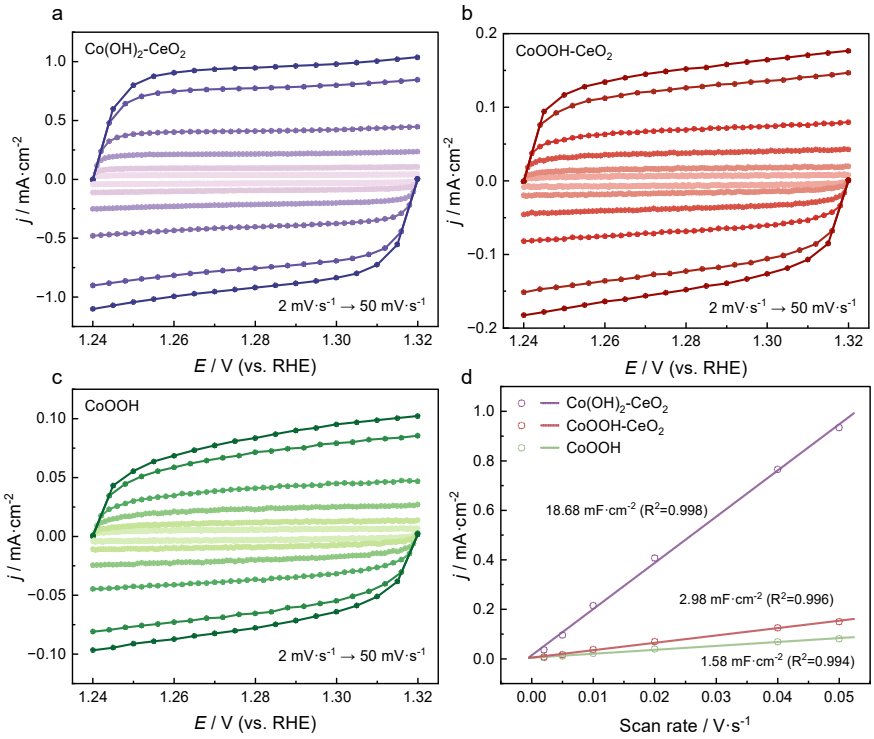

Figure S13. Voltammetric curves of (a) $Co(OH)_2$-CeO_2, (b) CoOOH-CeO_2 and (c) CoOOH obtained at different scan rates in non-Faradaic region. (2 $mV·s^{-1}$, 5 $mV·s^{-1}$, 10 $mV·s^{-1}$, 20 $mV·s^{-1}$, 40 $mV·s^{-1}$ and 50 $mV·s^{-1}$) (d) Plots of the change in half of the difference between positive and negative scanning current densities with different scan rates. The double-layer capacitance was obtained from the slope of the fitted line.[3]

Note: Deposition of CeO_2 did not significantly alter the morphology of $Co(OH)_2$ or CoOOH (Fig. S3 and S4). Notably, CeO_2 prevented the $Co(OH)_2$-CeO_2 heterostructure from transforming into thick hexagonal nanosheets after OER redox process. The retained thin morphology offers a larger specific surface area, which is generally associated with more effective exposure of active sites, higher double-layer capacitance (C_{dl}), and an increased electrochemical active area.

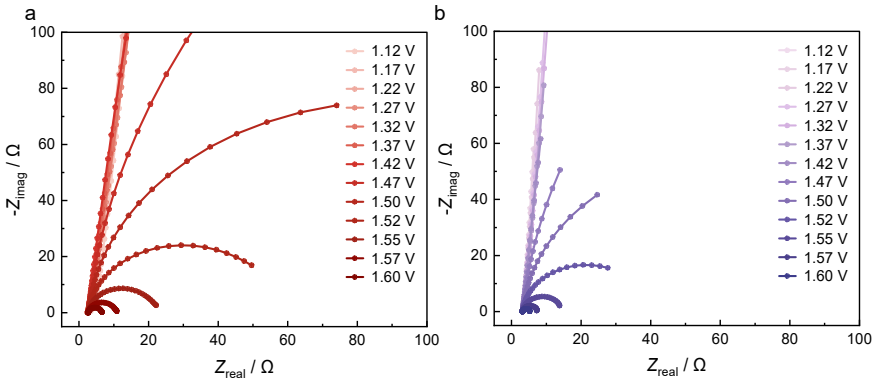

Figure S14. Nyquist plots of (a) CoOOH-CeO_2 and (b) $Co(OH)_2$-CeO_2 at different potentials.

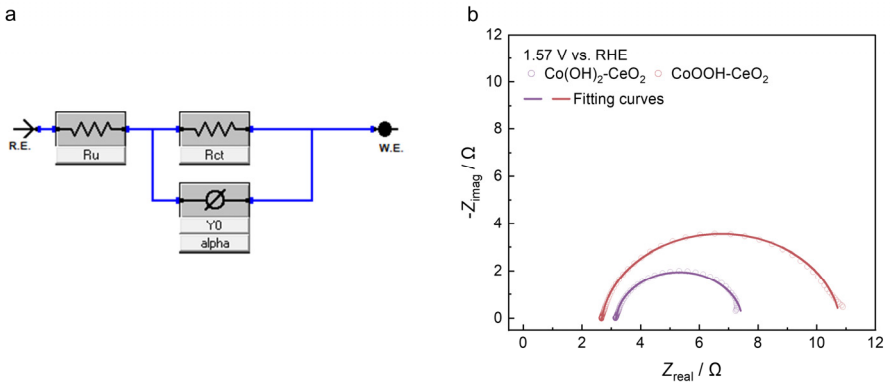

Figure S15. (a) Equivalent circuit diagram for fitting. (b) Nyquist plots of $Co(OH)_2$-CeO_2 and CoOOH-CeO_2 at 1.57 V vs. RHE. Fitting results and errors were shown in Table S1.

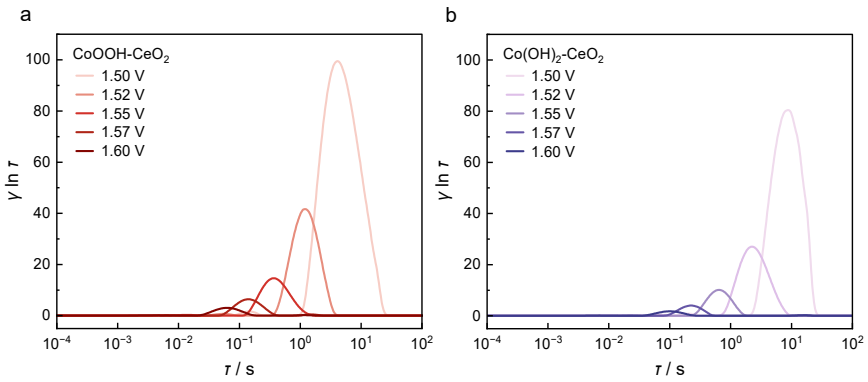

Figure S16. Potential dependence of DRT spectra of (a) CoOOH-CeO_2 and (b) $Co(OH)_2$-CeO_2. DRT data were obtained using the DRTtools developed by Wan et al. based on the Matlab programming language.[11]

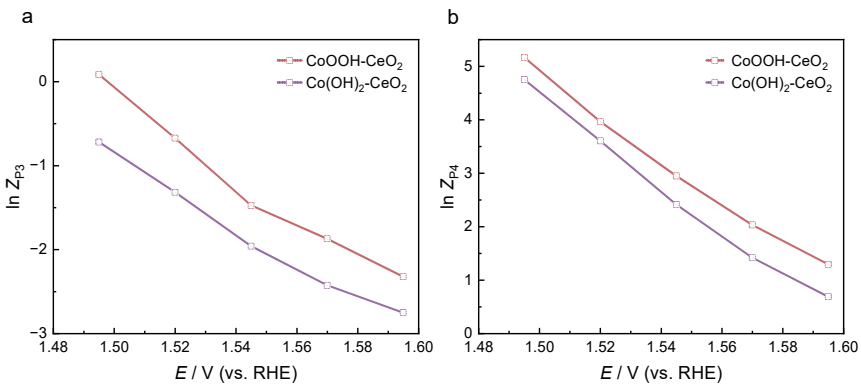

Figure S17. DRT analysis of (a) P3 and (b) P4 during OER potentials.

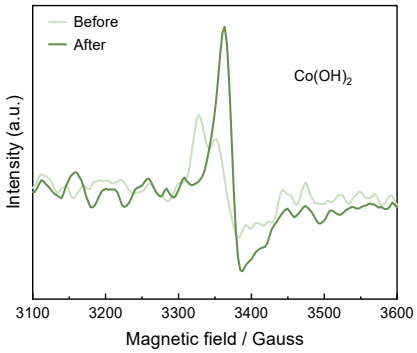

Figure S18. EPR spectra of $Co(OH)_2$ before and after OER redox cycles.

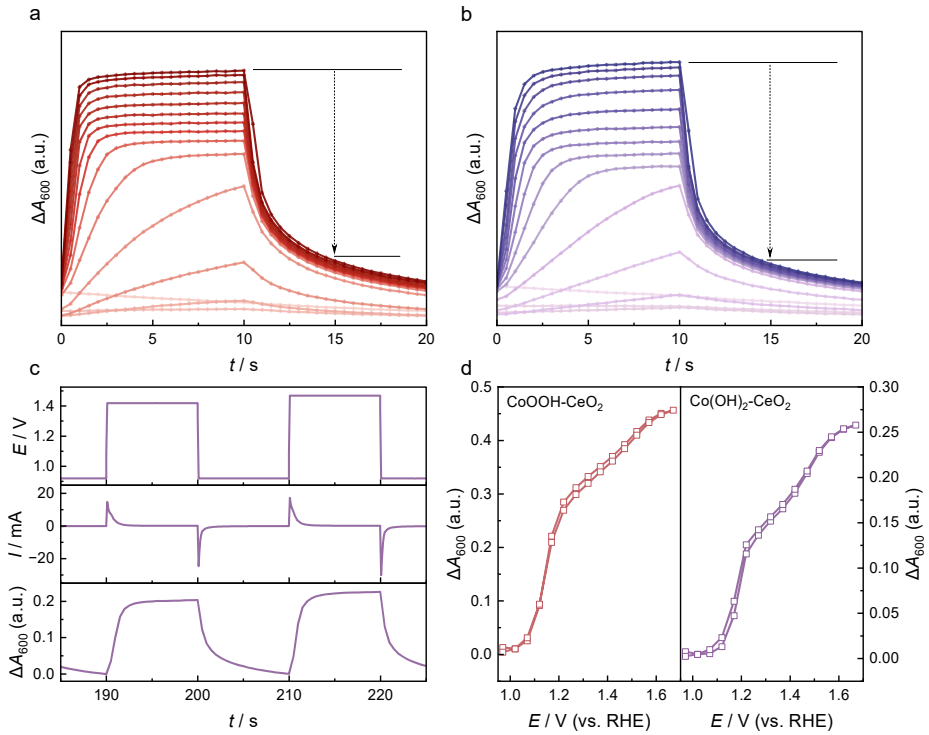

Figure S19. Variation of absorbance of (a) CoOOH-CeO_2 and (b) $Co(OH)_2$-CeO_2 at a fixed wavelength of 600 nm under pulsed potentials. (c) Electrochemical protocols for in situ UV-Vis measurements. (f) The optical absorption response of CoOOH-CeO_2 (left) and $Co(OH)_2$-CeO_2 (right) at 600 nm at various applied potentials.

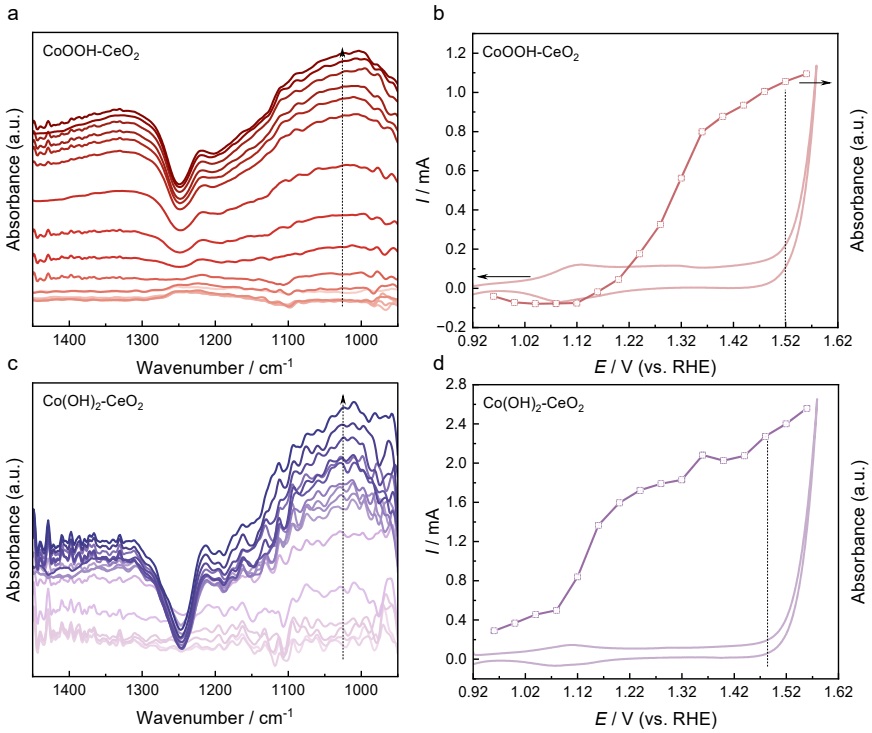

Figure S20. In situ ATR-SEIRAS spectra of (a) CoOOH-CeO_2 and (c) $Co(OH)_2$-CeO_2 at various applied potentials. (c) Absorbance variations (extracted at 1025 cm^{-1}) of (b) CoOOH-CeO_2 and (d) $Co(OH)_2$-CeO_2 at various applied potentials. CV curves under the same conditions were represented by light-colored lines. The dashed lines indicate the onset potential used for normalization.

Note: The band at 1000-1100 cm^{-1} is assigned to surface oxygen intermediates (e.g., Co-OOH or Co-OO*), consistent with prior ATR-SEIRAS and computational reports.[12-16] Because our conclusion concerns the relative accumulation of oxygen-containing intermediates rather than their exact speciation. The absorbance at 1025 cm^{-1} is extracted to represent the quantitative change in intermediates at each potential.

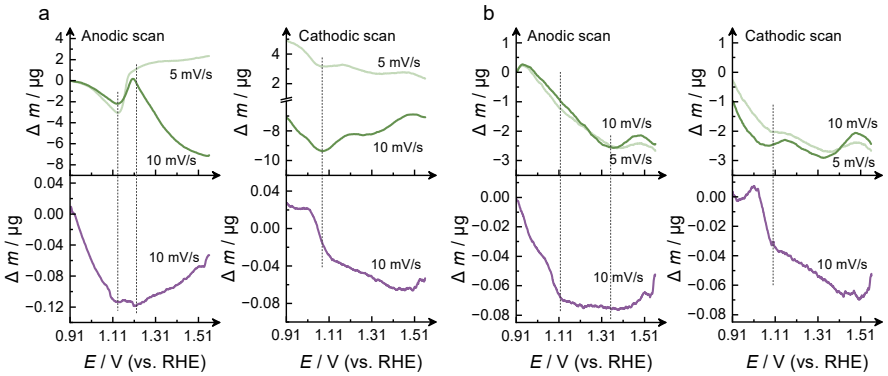

Figure S21. Mass changes of $Co(OH)_2$ (upper panel, green lines) and $Co(OH)_2$-CeO_2 (lower panel, purple lines) during the (a) first and (b) fifth CV cycles were recorded by eQCM. For $Co(OH)_2$, experiments at different scan rates demonstrated a scan-rate-dependent trend in mass loss.

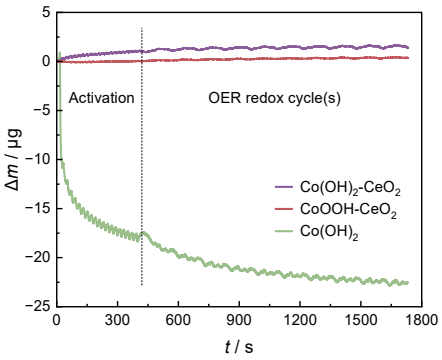

Figure S22. Simulated mass changes of three electrocatalysts during activation and OER redox cycles.

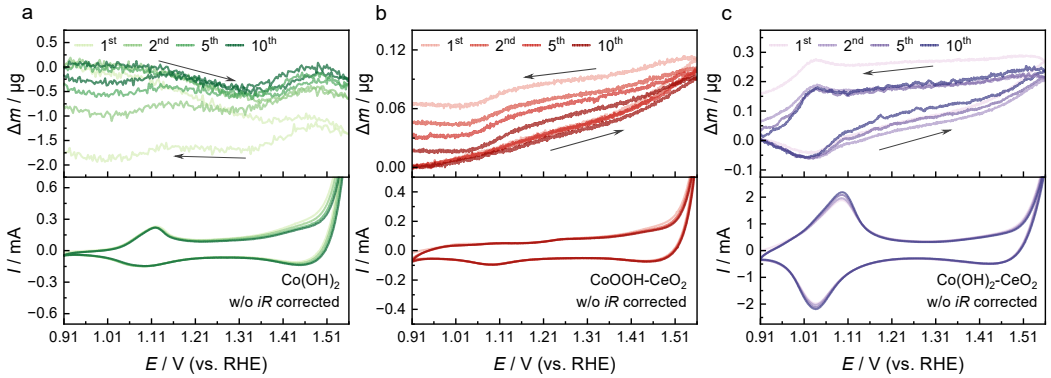

Figure S23. Mass changes (upper panel) of (a) $Co(OH)_2$, (b) $CoOOH\text{-}CeO_2$ and (c) $Co(OH)_2\text{-}CeO_2$ during OER redox cycles, extracted from Figure S21, with corresponding polarization curves shown in the lower panel.

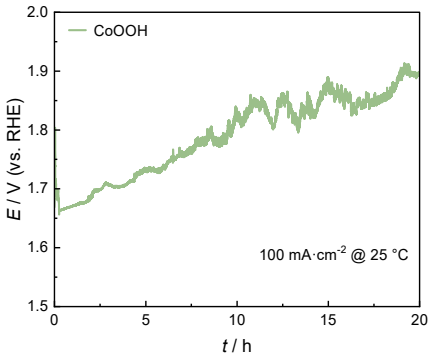

Figure S24. Chronopotentiometry test of CoOOH/CP at 100 mA·cm^{-2}.

3. Supplementary Tables

Table S1. The fitted EIS parameters and errors of CoOOH-CeO_2 and $Co(OH)_2$-CeO_2 at 1.57 V vs. RHE.

	R_u /Ω	Error /Ω	R_{ct} /Ω	Error /Ω	Y_0 /(S·s$^{\alpha}$)	Error /(S·s$^{\alpha}$)	α	Error	Goodness of Fit
CoOOH-CeO_2	2.676	0.0099	8.117	0.084	0.021	0.0005	0.92	0.008	6.16E-05
$Co(OH)_2$-CeO_2	3.162	0.0112	4.303	0.066	0.056	0.0018	0.93	0.013	4.63E-05

Table S2. Comparison of our work with prior studies.

Heterostructure	Substrate (the primary phase)	The secondary phase	$\Delta\eta_{10}$ /mV	Substrate Type	Reference
CeO_2/$Ni(OH)_2$	$Ni(OH)_2$	CeO_2	30↓	Dynamic	17
$CoS_{1.97}$-CeO_2	$CoS_{1.97}$(or $Co(CO_3)_{0.5}(OH)\cdot 0.11H_2O$)	CeO_2	40↓	Dynamic	18
$Co(OH)_2$-CeO_2	$Co(OH)_2$	CeO_2	46↓	Dynamic	This work
CeO_x/CoO_x	CoO_x	CeO_x	18↓	Static	19
NiO/CeO_2	NiO	CeO_2	20↓	Static	20
$NiFeO_x$/CeO_x	$NiFeO_x$	CeO_x	10↑	Static	21
CoOOH-CeO_2	CoOOH	CeO_2	16↓	Static	This work
CeO_2/$Co(OH)_2$	CeO_2	$Co(OH)_2$	-	Static	22

Note: We interpret prior reports within our framework and find that when CeO_2 is deposited on substrates with dynamic reconstruction potential (e.g., hydroxides and sulfides), larger reductions in overpotential are commonly observed, whereas static substrates yield modest reductions. Here, the concept of dynamic vs. static substrates is introduced. We provides a mechanistic explanation for the two distinct enhancement regimes reported for CeO_2-based heterostructures. The work by Sung et al.[22] offers a complementary perspective: $Co(OH)_2$ is deposited onto CeO_2 which acts as a static substrate in our framework. Because isolated CeO_2 is often considered catalytically inactive, quantifying overpotential reduction in that configuration is less straightforward. In summary, the performance of heterostructures is not simply additive and rational design principles are required.

4. References

1 L. Yang, R. Liu and L. Jiao, *Adv. Funct. Mater.*, 2020, **30**, 1909618.
2 Y. Liang, Y. Li, H. Wang, J. Zhou, J. Wang, T. Regier and H. Dai, *Nat. Mater.*, 2011, **10**, 780–786.
3 C. C. L. McCrory, S. Jung, J. C. Peters and T. F. Jaramillo, *J. Am. Chem. Soc.*, 2013, **135**, 16977–16987.
4 W. Shen, Y. Ye, Y. Hu, H. Wu, Q. Xia, H. Xie, Z. Li, N. Zhang, L. An, R. Si, P. Xi and C.-H. Yan, *J. Am. Chem. Soc.*, 2025, **147**, 17190–17200.
5 J. Du, J. Morales-Santelices, O. Y. Bisen, D. Antipin, D. M. Morales and M. Risch, *Electrochim. Acta*, 2025, **512**, 145489.
6 J. Yang, H. Liu, W. N. Martens and R. L. Frost, *J. Phys. Chem. C*, 2010, **114**, 111–119.
7 S. Wang, Q. Jiang, S. Ju, C.-S. Hsu, H. M. Chen, D. Zhang and F. Song, *Nat. Commun.*, 2022, **13**, 6650.
8 P. Ma, H. Cao, Q. Hao, R. Wang, W. Liu, M. Zuo, C. Jia, Z. Zhang and J. Bao, *Angew. Chem., Int. Ed.*, 2024, **63**, e202404418.
9 Z. Zhang, F. Zhang, Y. Cui, W. Luo, M. Shu, S. Wang, Z. Lu, Y. Hou and R. Hao, *J. Am. Chem. Soc.*, 2025, **147**, 23617–23624.
10 C. Jing, T. Yuan, L. Li, J. Li, Z. Qian, J. Zhou, Y. Wang, S. Xi, N. Zhang, H.-J. Lin, C.-T. Chen, Z. Hu, D.-W. Li, L. Zhang and J.-Q. Wang, *ACS Catal.*, 2022, **12**, 10276–10284.
11 T. H. Wan, M. Saccoccio, C. Chen and F. Ciucci, *Electrochim. Acta*, 2015, **184**, 483–499.
12 M. Zhang, M. de Respinis and H. Frei, *Nat. Chem.,* 2014, **6**, 362–367.
13 C. Lang, J. Li, K. R. Yang, Y. Wang, D. He, J. E. Thorne, S. Croslow, Q. Dong, Y. Zhao, G. Prostko, G. W. Brudvig, V. S. Batista, M. M. Waegele and D. Wang, *Chem*, 2021, **7**, 2101–2117.
14 L. Zeng, Z. Zhao, F. Lv, Z. Xia, S.-Y. Lu, J. Li, K. Sun, K. Wang, Y. Sun, Q. Huang, Y. Chen, Q. Zhang, L. Gu, G. Lu and S. Guo, *Nat. Commun.*, 2022, **13**, 3822.
15 L. Jiang, Y. Hao, M. Gu, L. Deng, Q. Chen, X. Zhang, L. Li, S. Peng and G. Wang, *Angew. Chem., Int. Ed.*, 2025, **64**, e202423145.
16 G. Gao, G. Li, T. Huang, J. Wan, Z. Geng, H. Tang, X. Zhao, S. Fu, L. Sun, J. Li and L. Li, *J. Am. Chem. Soc.*, 2025, **147**, 29767–29778.
17 Z. Liu, N. Li, H. Zhao, Y. Zhang, Y. Huang, Z. Yin and Y. Du, *Chem. Sci.*, 2017, **8**, 3211–3217.
18 T. Dai, X. Zhang, M. Sun, B. Huang, N. Zhang, P. Da, R. Yang, Z. He, W. Wang, P. Xi and C.-H. Yan, *Adv. Mater.*, 2021, **33**, 2102593.
19 J.-H. Kim, K. Shin, K. Kawashima, D. H. Youn, J. Lin, T. E. Hong, Y. Liu, B. R. Wygant, J. Wang and G. Henkelman and C. B. Mullins, *ACS Catal.*, 2018, **8**, 4257–4265.
20 J. Yu, Q. Cao, Y. Li, X. Long, S. Yang, J. K. Clark, M. Nakabayashi, N. Shibata and J.-J. Delaunay, *ACS Catal.*, 2019, **9**, 1605–1611.
21 K. Obata and K. Takanabe, *Angew. Chem., Int. Ed.*, 2018, **57**, 1616–1620.
22 M.-C. Sung, G.-H. Lee and D.-W. Kim, *J. Alloys Compd.*, 2019, **800**, 450–455.